American Journal of Energy Engineering
2025, Vol. 13, No. 4, pp. 158-170
https://doi.org/10.11648/j.ajee.20251304.11

Research Article

Design Window for SHJ Cells: Joint Impact of Base Thickness and Doping Under AM1.5G

Jacques Joachim Faye, Aly Toure, Mamadou Lamine Samb*, Dimity Diassy

Department of Physics and Chemistry, University Iba Der Thiam of Thies, Thies, Senegal

Abstract

We numerically map the joint impact of base thickness (e) and donor density (N_D) on silicon heterojunction (SHJ) cells under AM1.5G using SILVACO ATLAS (drift–diffusion with SRH/Auger and field/concentration-dependent mobilities). Optics is treated by 2D specular ray tracing (no texturing), so results constitute a conservative baseline at small e. To isolate e and N_D, the a-Si:H/c-Si interface is held fixed across parameter sweeps. We identify an absorption–collection trade-off: J_{sc} increases from thin to moderate e and then saturates or declines; V_{oc} decreases with increasing e and high N_D due to enhanced recombination. The fill factor peaks at small e under low-to-moderate N_D. Efficiency exhibits a robust optimum at moderate thickness (e.g., $e \approx$ 120-160μm) and intermediate N_D, whereas heavy doping shifts the optimum but ultimately degrades V_{oc}/FF via Auger (and, in extended models, band-gap narrowing). From a design standpoint, we delineate a practical window that balances resistivity and recombination while avoiding heavy doping. Limitations: absence of light trapping and fixed interface, mean our absolute metrics are conservative, but trends and optima are robust. Planned extensions include Lambertian/textured optics, interface sweeps, and calibrated BGN/contact models to raise absolute values without altering the identified trade-offs.

Keywords

SHJ/HIT Solar Cell, Silicon, TCAD, Thickness, Doping, J_{sc}, V_{oc}, Fill Factor, Efficiency

1. Introduction

Silicon heterojunction (SHJ/HIT) solar cells pair a crystalline silicon (c-Si) wafer with ultrathin a-Si:H layers that deliver excellent surface passivation and selective, transparent contacts, enabling very high V_{oc}, record FF, and certified efficiencies beyond 26% on industrial wafers [1–4]. As records approach the intrinsic c-Si limit under AM1.5G (~29%), understanding losses and design trade-offs becomes critical [5]. Two tightly coupled levers dominate: wafer thinning and base-doping optimization. Thinning reduces material use and transport lengths but can increase NIR escape without light-trapping, lowering J_{sc} if not mitigated [6]. Base doping governs resistivity and recombination; at high density, Auger processes strengthen and band-gap narrowing (BGN) emerges, shaping V_{oc}, FF, and η [7, 8].

Here we map the joint influence of base thickness $e\ (20-400\ \mu m)$ and donor density $N_D\ (10^{14}-1\times 10^{17}\ cm^{-3})$ via TCAD (SILVACO ATLAS, 300 K, AM1.5G). Optics uses 2D specular ray-tracing (SOPRA n, k for Si/Al/ITO/a-Si:H/a-SiC) without texturing to provide a conservative J_{sc} bound; the a-Si:H/c-Si interface is fixed to isolate e and N_D. SRH and Auger recombination with Fermi statistics and field/concentration-dependent mobilities are

*Corresponding author: mlsamb@univ-thies.sn (Mamadou Lamine Samb)

Received: 9 October 2025; **Accepted:** 17 October 2025; **Published:** 31 October 2025

enabled; J_{sc}, V_{oc}, FF, and η are extracted from simulated $J-V$ curves. The results identify optimal ranges of thickness and doping, explain trends via the absorption-collection trade-off and concentration-dependent recombination, and position the outcomes relative to recent records and physical limits [1–5].

2. Electrical Modeling of a Solar Cell

2.1. Electrical Characteristics (Single-diode Model)

The equivalent circuit of a photovoltaic (PV) cell (Figure 1) consists of a photocurrent source I_{ph} in parallel with a diode, together with a series resistance R_s (internal ohmic losses: metallization, TCO, semiconductor) and a shunt resistance R_s (leakage currents due to recombination and bypass paths). This single-diode model is the standard compact description of the illuminated $I-V$ curve and of performance parameters (J_{sc},V_{oc},FF,η) [9, 10].

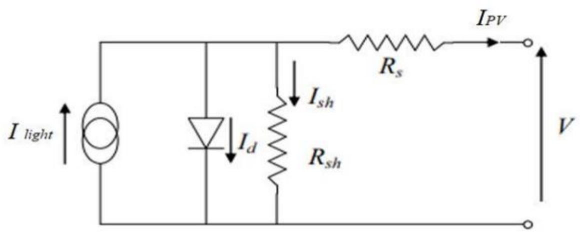

Figure 1. *Equivalent circuit of a PV cell (source I_{ph}, diode, R_s, R_{sh}).*

Under illumination, the nodal equation reads:

$$I_{PV} = I_{ph} - I_d - I_{sh} \tag{1}$$

where I_d is the diode current and I_{sh} the current through the shunt branch.

The diode current follows the Shockley equation including the series ohmic drop:

$$I_d = I_0 \left[exp\left(\frac{V_d}{AV_t}\right) - 1\right] \tag{2}$$

while the shunt current is:

$$I_{sh} = \frac{V+I_{PV}R_s}{R_{sh}} \tag{3}$$

with $\mathrm{I_0}$ the reverse saturation current of the diode, n the ideality factor (≈ 1–2), and $\mathrm{V_T} = \frac{\mathrm{k_B T}}{\mathrm{q}}$ the thermal voltage $\mathrm{k_B}$: Boltzmann constant, T: absolute temperature, q: elementary charge). Combining (1)-(3) yields the implicit $\mathrm{I-V}$ equation of the single-diode model with $\mathrm{R_s}$and $\mathrm{R_{sh}}$:

$$I_{PV} = I_{ph} - I_0 \left[exp\left(\frac{V+I_{PV}R_s}{nV_T}\right) - 1\right] - \frac{V+I_{PV}R_s}{R_{sh}} \tag{4}$$

These relations underpin five-parameter PV module models and associated identification methods (translation across STC/NOCT, temperature/irradiance extrapolation). Analytical forms and closed-form solutions (e.g., using the Lambert W function) exist for evaluating I(V), yet numerical solution of the implicit (4) is common in simulation practice [10]. For performance analysis, one extracts: J_{sc} (at $V=0$), V_{oc} (at $I_{ph}=0$), the fill factor (FF), and the efficiency (η). (in current-density form, with G the AM1.5G irradiance).

Note that R_s tends to reduce FF (rounding the $I-V$ knee), while a low R_{sh} increases the slope near short-circuit and degrades J_{sc}/FF [10].

2.2. J–V Characteristic of a Solar Cell

A cell's performance is assessed from its current–voltage characteristic $J(V)$ under illumination (Figure 2). From this curve one extracts the standard PV figures of merit: the short-circuit current density J_{sc}, the open-circuit voltage V_{oc}, the fill factor FF, and the efficiency η [11]. The power curve is $P(V) = V\,J(V)$; its maximum at the maximum power point (V_m,J_m) characterizes the cell's conversion capability.

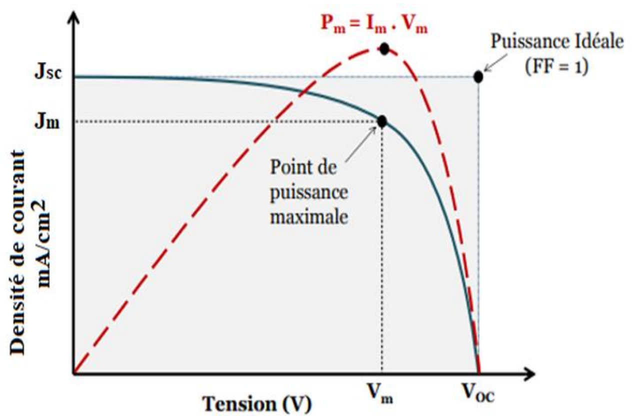

Figure 2. *J(V) characteristic and power curve of a photovoltaic cell [12].*

2.2.1. Short-circuit Current Density J_{sc}

By definition, $J_{sc} = J(V=0)$. Under short circuit, photogenerated carriers are separated by the internal field and collected at the contacts; the current is limited by

1) optical losses (front-surface reflection, transmission, parasitic absorption in front layers/encapsulation) and
2) electrical collection, notably the minority-carrier diffusion length and bulk/surface recombination.

In the linear regime, J_{sc} increases approximately proportionally with irradiance, consistent with its integral definition via the EQE:

$$J_{sc} = q \int_{\lambda} \Phi_{AM1,5G}(\lambda)\, EQE(\lambda) d \quad (5)$$

$$STG, G = 1000\, Wm^{-2}$$

where $\Phi_{AM1,5G}$ is the photon spectral flux specified by IEC 60904-3 [11].

2.2.2. Open-circuit Voltage V_{oc}

Voc is the voltage that drives the net current to zero ($J = 0$): the photogenerated polarization exactly balances the diode current. In the limit $R_S \to 0$ and $R_{sh} \to \infty$ (single-diode model), one obtains the classical expression [9]:

$$V_{oc} \simeq nV_T \ln\left(\frac{J_{sc}}{J_0} + 1\right) \quad (6)$$

with J_0 the saturation current, n the ideality factor ($\approx 1-2$), and $V_T = k_B T/q$ the thermal voltage. This highlights the sensitivity of V_{oc} to recombination (which sets J_0).

2.2.3. Fill Factor FF

By definition,

$$FF = \frac{J_m V_m}{J_{sc} V_{oc}} \quad (7)$$

where (J_m, V_m) denotes the maximum power point. FF decreases when series resistance R_s increases (rounding of the knee) and when shunt resistance R_{sh} decreases (larger slope near short circuit) [10]. For an ideal diode (no R_s, R_{sh}), a useful analytic approximation links FF to $v_{oc} = V_{oc}/(nV_T)$ [10]:

$$FF \approx \frac{v_{oc} - \ln(v_{oc} + 0{,}72)}{v_{oc} + 1} \quad (8)$$

often used for quick estimates of the FF limit from V_{oc}.

2.2.4. Power Conversion Efficiency η

The efficiency is the ratio of the maximum electrical power delivered by the cell to the incident power per unit area. In current-density form,

$$\eta = \frac{J_m V_m}{G} = \frac{J_{sc} V_{oc} FF}{G} \quad (9)$$

where G is the irradiance. Under standard test conditions (STC), $G = 1000\ \mathrm{W\,m^{-2}}$ and the spectrum is AM1.5G as defined by IEC 60904-3 [11]. This expression makes explicit the multiplicative contributions of J_{sc}, V_{oc}, and FF to overall performance.

3. Simulation Parameters

3.1. Device Architecture

We model a classical crystalline-silicon heterojunction (SHJ) solar cell in which a crystalline-Si (c-Si) base is sandwiched between thin, highly doped hydrogenated amorphous-Si layers: a front p+ a-Si:H emitter (FSF) and a rear n+ a-Si:H back-surface field (BSF). This multilayer stack (p+)-a-Si:H/(n)-c-Si/(n+)-a-Si:H is widely used to combine excellent surface passivation with selective carrier transport and has enabled state-of-the-art device efficiencies above 26% in large-area cells. [3, 13, 14]

A schematic of a conventional heterojunction photovoltaic (PV) solar cell is shown in Figure 3.

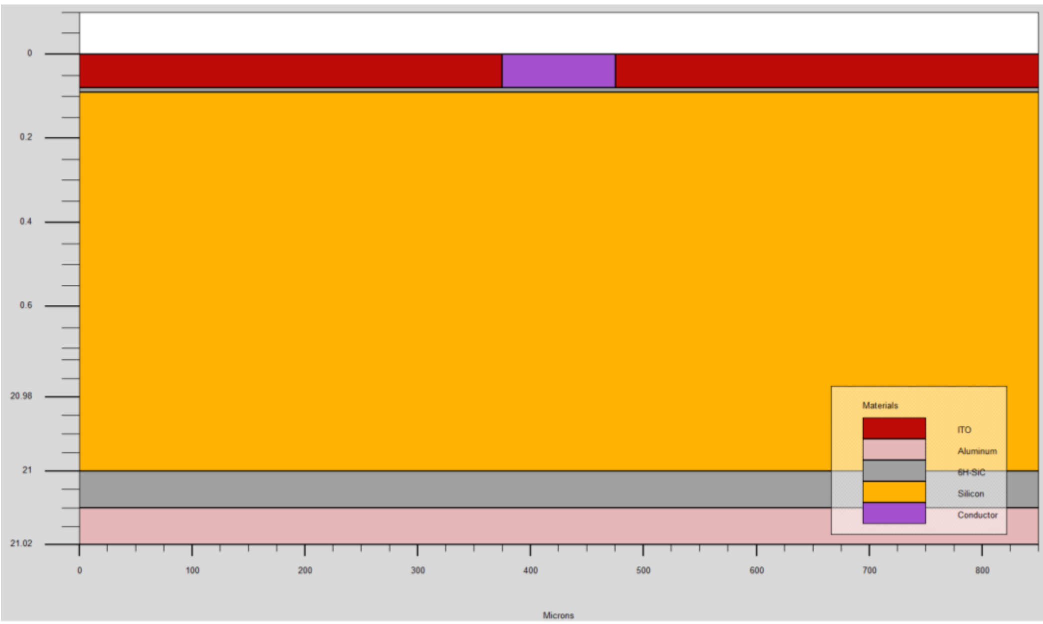

Figure 3. Schematic structure of the heterojunction PV solar cell to be simulated.

3.2. Simulation Environment and Governing Physics

All simulations are performed with SILVACO ATLAS at $T = 300\,K$. We solve Poisson's equation self-consistently with the electron and hole continuity equations. Recombination includes Shockley–Read–Hall (SRH) and Auger mechanisms; Fermi statistics are used. Field- and concentration-dependent mobility models (keywords fldmob/conmob) are enabled. Unless stated otherwise, contacts are ohmic with a contact resistivity of $0.5\,\Omega \cdot cm^2$ and surface recombination velocities $s_n = s_p = 10^5\,cm\,s^{-1}$. (General ATLAS methodology and usage of v5.28.1. R are documented and broadly adopted in recent device-simulation studies.) [15-17].

3.3. Optical Model and Illumination Conditions

The optical response is computed via 2D specular ray-tracing under AM1.5G illumination with an incident irradiance of $100\,mW\,cm^{-2}$ (STC). Optical constants n, k for Si, Al, ITO, and a-Si:H/a-SiC are taken from the SOPRA database. No Lambertian texturing is included in this baseline (front and rear reflections are treated as specular, front. refl/back. refl). A front aluminum grid (100 µm wide over an 850 µm 2D pitch) is included, causing ≈12% geometric shading. AM1.5G and STC conventions follow IEC 60904-3: 2019. [4, 5, 11, 18].

3.4. Interface and Defect Modeling (Scope of this Work)

Because SHJ performance is very sensitive to interfacial dangling-bond states at the a-Si:H/c-Si junction, we acknowledge that the interface defect density Dit and capture cross-sections σ_n/σ_p critically affect V_{oc} and FF. To isolate the causal impact of base thickness e and base doping N_D, we keep the interface model fixed throughout this study (parameters summarized in Table 2) and do not sweep Dit or σ\sigmaσ. This choice preserves the relative trends we report; absolute values may shift when interface parameters are re-optimized. A dedicated follow-up will explicitly vary Dit, σ_n/σ_p, and passivation conditions. [19].

3.5. Study Plan, Outputs, and Interpretation Note on High J_{sc} at $e \approx 30\,\mu m$

We sweep the c-Si base thickness e and donor density $N_D \in [10^{14}, 10^{17}]\,cm^{-3}$, keeping all other layers and dopings fixed. From illuminated $J - V$ curves over $0 - 1\,V$, we extract the figures of merit: J_{sc}, V_{oc}, fill factor (FF), and efficiency η; is normalized to $100\,mW\,cm^{-2}$. As a methodological note: a high J_{sc} observed near $e \approx 30\,\mu m$ can be physically consistent with:

1) reduced bulk recombination due to the shorter carrier transport path in thin wafers, provided lifetime remains high, and
2) still-adequate absorption across the blue/visible spectrum where Si is strongly absorbing; the remaining near-IR deficit is mitigated if front-surface parasitics (a-Si:H/TCO) are controlled.

Our specular model likely underestimates absolute J_{sc} versus textured devices but preserves the thickness trend, which is consistent with light-trapping literature and with quantified front-stack parasitic-absorption analyses in SHJ [2, 11, 13, 18, 20].

3.6. Material Parameters Used in the Device Deck

Table 1. *Material Parameters Used in the Simulation.*

Different Layers Physical Properties	**FSF (a-Si:H)**	**Substrate (c-Si)**	**BSF (a-Si:H)**	**Units**
Thickness	0,1	250	0,1	(μ_m)
Bandgap (E_g)	1,7	1,12	1,7	(eV)
Electron affinity (χ)	3,9	4,05	3,9	(eV)
Electron lifetime τ_n	1.10^{-6}	1.10^{-3}	1.10^{-6}	S
Hole lifetime τ_p	1.10^{-6}	1.10^{-3}	1.10^{-6}	S
Electron mobility μ_n	1	1	1350	$cm^2/V.s$
Hole mobility μ_p	0.5	0.5	450	$cm^2/V.s$
N_c(eff. DOS, CB)	2.10^{20}	$2,8.10^{19}$	2.10^{20}	cm^2

Different Layers Physical Properties	FSF (a-Si:H)	Substrate (c-Si)	BSF (a-Si:H)	Units
N_v((eff. DOS, VB))	2.10^{20}	$1{,}04.10^{19}$	2.10^{20}	cm^2
Relative permittivity ε_r	11,9	11,9	11,9	

Parasitic front-stack absorption and its impact on J_{sc} are consistent with SHJ measurements and modelling [5, 13].

The defects present in the two thin hydrogenated amorphous silicon layers of the BSF and the varied front emitter are listed in Table 2 below.

***Table 2.** Simulation Parameters of Defect State Densities and Electron (Hole) Capture Cross-Sections.*

Quantity	"A" (acceptor-like)	"D" (donor-like)	Units
Gaussian DOS peak N_{GA}, N_{GD}	$1{,}5.10^{15}$	$1{,}5.10^{15}$	cm^{-3}
Tail DOS prefactor N_{TA}, N_{TD}	1.10^{21}	1.10^{21}	cm^{-3}
Gaussian peak energy E_{GA}, E_{GD}	0,62	0,78	Ev
Gaussian width W_{GA}, W_{GD}	0,15	0,15	Ev
Tail width W_{TA}, W_{TD}	0.033	0.049	Ev
Electron capture σ_n	1.10^{-17}	1.10-^{15}	cm^{-2}
Hole capture σ_P	1.10^{-15}	1.10^{-17}	cm^{-2}

3.7. Extraction and Reporting

Figures of merit $\{J_{sc}, V_{oc}, FF, \eta\}$ are extracted from the simulated illuminated $J - V$ curves $(0 - 1\,V)$. Efficiency η is computed with input power fixed at $100\,mW\,cm^{-2}$. Where discussed, we reference recent SHJ performance records (Kaneka IBC-SHJ >26% and subsequent 26.81% SHJ reports) solely as context for plausible ranges and trade-offs in J_{sc}, V_{oc}, and FF under modern front-stack designs [3, 14, 21].

3.8. Choice of Parameter Ranges

We sweep the base thickness $e = 20 - 400\,\mu m$ to span ultra-thin wafers (material savings, stronger transport constraints) up to standard industrial thickness, capturing the visible/NIR absorption transition without texturing. The donor density is varied over $N_D = 1 \times 10^{14} - 1 \times 10^{17}\,cm^{-3}$ to cover the regime from lightly doped (series-resistance limited) to moderately heavy doping where Auger recombination and band-gap narrowing (BGN) begin to penalize V_{oc} and FF. These bounds reflect current SHJ practice and common TCAD modeling windows, ensuring both relevance and physical realism. 4. Results and Discussion.

4. Effect of Substrate Donor Density for Different Base Thicknesses

4.1. Impact on the Short-circuit Current Density (J_{sc})

Under AM1.5G, the short-circuit current density is given by equation (5) and results from a balance between optics (spectral absorption, front-side parasitics) and electrical collection (transport vs. recombination). In our specular optical framework (no Lambertian texturing) with ≈ 12% front-grid shading, J_{sc} is set by strong visible absorption and efficient bulk collection, while NIR absorption losses become significant at very small thickness [3, 13].

Figure 4 illustrates the evolution of J_{sc} as a function of the donor density N_D for different base thicknesses e $(20 - 400\,\mu m)$ under AM1.5G, using a specular optical model and keeping the a-Si:H/c-Si interface fixed. A quasi-plateau around $J_{sc} \approx 38.4\,mA\,cm^{-2}$ is observed for $e \geq 80\,\mu m$ at moderate doping, followed by a clear decrease beyond $N_D \approx 5 \times 10^{15}\,cm^{-3}$.

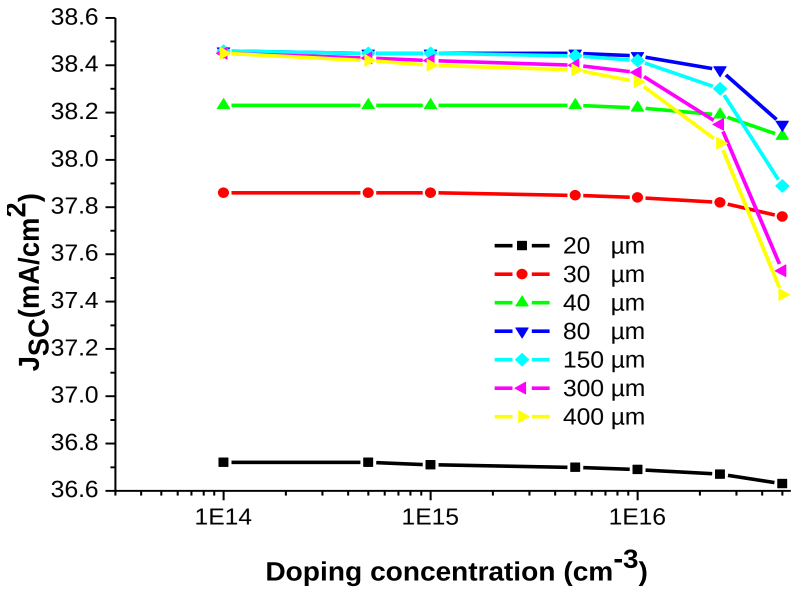

Figure 4. *Variation of the short-circuit current density J_{sc} of an SHJ cell versus N_D (substrate) for different base thicknesses e.*

An examination of Figure 4 reveals that:

1) Thin bases yield the lowest J_{sc}: $20\ \mu m$ (lowest), then $30\ \mu m$. The main cause is incomplete near-IR absorption in a specular model (short optical path) despite favorable carrier collection due to shorter transport distances [4, 5].
2) For moderate doping $N_D \in [1\times10^{14}, 5\times10^{15}]\ cm^{-3}$, a quasi-plateau at $Jsc \approx 38.4\ mA\ cm^{-2}$ appears for $80-400\ \mu m$: beyond $\sim 80\ \mu m$ (non-textured model), absorption is already near saturation and further thickness adds only a marginal photocurrent gain [4, 13].
3) From $N_D \approx 5\times10^{15}\ cm^{-3}$ upward, J_{sc} decreases markedly for all thicknesses. Heavy doping increases Auger recombination, shortens the minority-carrier diffusion length, and, in more complete models, induces band-gap narrowing (BGN); collection degrades more strongly in thicker bases (longer paths), hence the trend "the larger e, the lower J_{sc}" at high doping [7, 8].

These trends agree with recent literature on:

1) light trapping and absorption limits in thinned c-Si [4, 5],
2) front-stack parasitics in SHJ [13], and (iii) the growth of Auger/BGN at high doping [7, 8].

4.2. Impact on the Open-circuit Voltage (V_{OC})

Figure 5 illustrates the evolution of the open-circuit voltage V_{OC} as a function of the donor density N_D for different base thicknesses e $(20-400\ \mu m)$, under AM1.5G, using a specular optical model and keeping the a-Si:H/c-Si interface fixed.

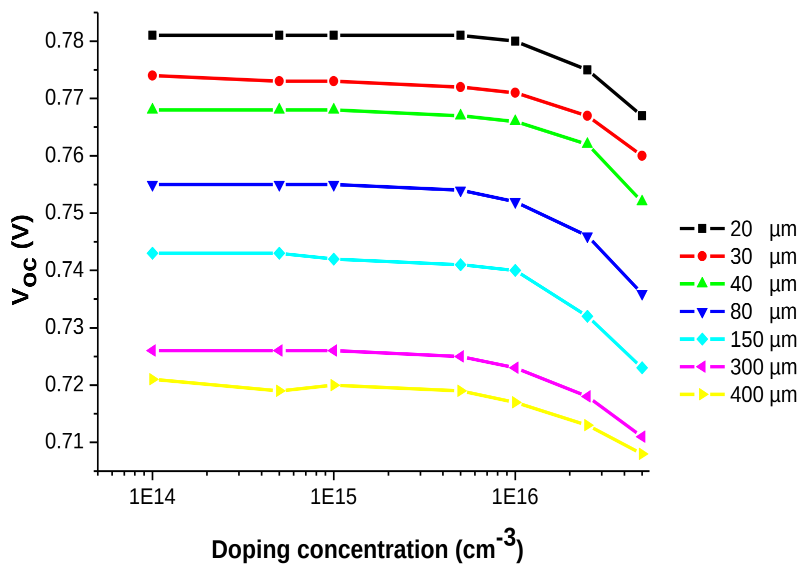

Figure 5. *Variation of V_{oc} of an SHJ cell versus N_D (substrate) for different base thicknesses e.*

An analysis of Figure 5 shows that:

1) For $N_D \in [10^{14}, 10^{16}]\ cm^{-3}$, V_{OC} is nearly constant for all thicknesses considered.
2) Beyond $N_D \approx 10^{16}\ cm^{-3}$, V_{OC} decreases markedly for all thicknesses.
3) At low doping ($N_D = 10^{14}\ cm^{-3}$), thinning the base from 400 μm to 200 μm increases V_{OC} from 0.723 V to 0.781 V; at higher doping ($N_D = 5 \times 10^{16}\ cm^{-3}$), V_{OC} ranges from 0.708 V to 0.767 V depending on thickness.
4) The maximum observed value, $V_{OC} = 0.781\ V$, is obtained for $e = 20\ \mu m$ when N_D is moderate (1×10^{14}, 5×10^{14}, 1×10^{15}, $5 \times 10^{15}\ cm^{-3}$).

Physical interpretation.

The open-circuit voltage follows the usual approximation.

$$V_{oc} \simeq \frac{kT}{q} \ln\left(\frac{J_{sc}}{J_0} + 1\right) \quad (10)$$

where J_0 (saturation current) aggregates bulk (SRH, Auger) and interfacial recombination [6, 7].

1) Thickness effect. At low doping, reducing e decreases the active volume and transport paths, which lowers J_0 (less SRH bulk recombination) and raises V_{OC}, a typical trend for thinned c-Si devices with high-quality front/rear passivation [3].
2) Doping effect. At high doping, J_0 rises sharply due to Auger recombination (carrier-concentration dependent) and, in more complete models, band-gap narrowing (BGN). These mechanisms decrease V_{oc} irrespective of thickness, explaining the drop above $10^{16}\ cm^{-3}$ [6-8].
3) Consistency with J_{sc} and η. The maximum V_{oc} at small e (20 μm) does not necessarily coincide with a maximum J_{sc} (limited by NIR absorption in a specular model) or with the maximum efficiency η. The J_{sc} and η sections thus show optima at moderate thickness (≈ 30 μm), consistent with the absorption–recombination trade-off.

4.3. Impact on the Fill Factor (FF)

Consistent with 4.1.1 (J_{sc}) and 4.1.2 (V_{OC}), our simulations distinguish three doping regimes:

1) Low: $N_D \leq 10^{15}\ cm^{-3}$
2) Moderate: $5 \times 10^{15} - 1 \times 10^{16}\ cm^{-3}$
3) High: $\geq 1 \times 10^{16}\ cm^{-3}$ (onset of the marked V_{OC} drop); a systematic degradation of FF and η appears beyond $\sim 2.5 \times 10^{16}\ cm^{-3}$.

Increasing doping reduces the bulk share of the series resistance (higher base conductivity) but raises Auger recombination (and, in more complete models, band-gap narrowing, BGN), which degrades the differential slope around the MPP and thus FF [3, 7, 8, 13].

Figure 6 shows the variation of FF versus donor density N_D for different base thicknesses e (20 − 400 μm) using a specular optical model and a fixed a-Si:H/c-Si interface.

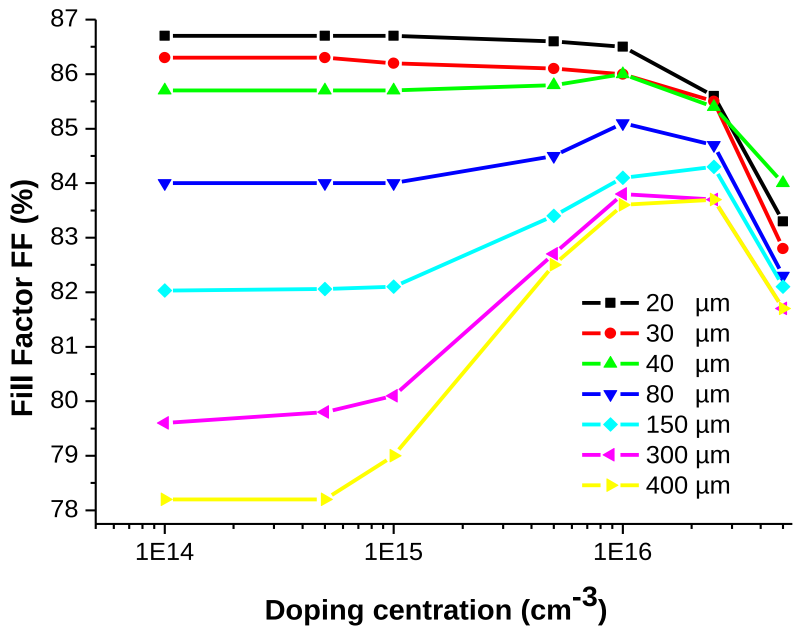

Figure 6. *Variation of the FF of an SHJ cell as a function of N_D for different base thicknesses.*

General trend from our simulations.

1) At low doping ($N_D \leq 10^{15}\ cm^{-3}$), thinning the base from 400 μm to 20 μm increases FF from ~78.2% to ~86.7%: collection improves (shorter transport

paths), the bulk component of R_S is smaller, and V_{OC} remains high (see 4.1.2).

2) At moderate doping $5 \times 10^{15} - 1 \times 10^{16}\ cm^{-3}$, FF stagnates or rises slightly depending on e: the conductivity gain can still outweigh added recombination.

3) At high doping $\geq 1 \times 10^{16}\ cm^{-3}$), Auger recombination dominates and FF decreases; beyond $2.5 \times 10^{16}\ cm^{-3}$, the drop becomes general across all thicknesses.

The maximum FF ($\approx$ 86.7%) occurs at $e = 20\ \mu m$ under low doping**,** consistent with the maximum V_{OC} at small e (4.1.2) and with the limitation of J_{sc} at $20\ \mu m$ by incomplete NIR absorption in a specular model (4.1.1).

4.4. Impact on Efficiency (η)

Efficiency $\eta = J_{sc} V_{oc} FF/G$

(with $G = 100\ mW\ cm^{-2}$, STC) reflects the combined trends of J_{sc}, V_{oc}, and FF [1, 16]. The near constancy of V_{oc} up to $\sim 10^{16}\ cm^{-3}$, the decrease of J_{sc} beyond $\sim 5 \times 10^{15}\ cm^{-3}$ (especially for large e), and the simultaneous drop of J_{sc} and V_{oc} for $N_D \gtrsim 10^{16}\ cm^{-3}$ explain the presence of an efficiency optimum at moderate thickness.

Figure 7 shows the evolution of the power conversion efficiency η as a function of the base donor density N_D for several base thicknesses e $(20 - 400\ \mu m)$ under the same modeling framework (specular optics, fixed interface).

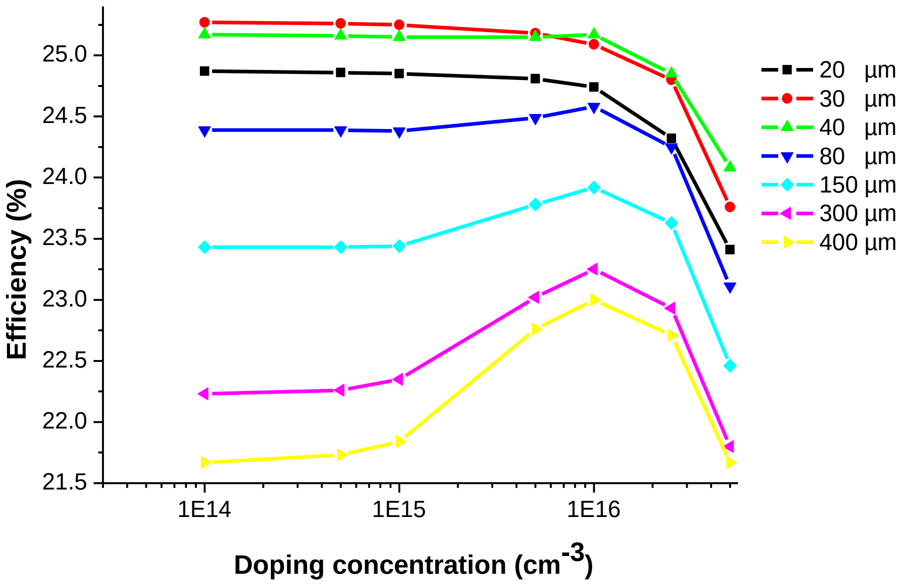

Figure 7. *Variation of the efficiency η of an SHJ cell versus N_D for different base thicknesses.*

Key results:

1) At $N_D \approx 10^{14}\ cm^{-3}$, thinning from 400 to $30\ \mu m$ increases η (~21.67% → ~25.17%): the absorption–transport balance is favorable. Below $30\ \mu m$, η decreases because J_{sc} is penalized by unabsorbed NIR (specular model without texturing) [13].

2) For $N_D \leq 10^{16}\ cm^{-3}$, η is broadly stable or slightly rising depending on e, as lower R_S (higher conductivity) can compensate.

3) At $N_D \geq 2.5 \times 10^{16}\ cm^{-3}$, η decreases for all thicknesses (Auger/BGN ⇒ lower V_{oc} and FF, smaller J_{sc}).

The observed optimum is $\eta \approx 25.17\%$ for $e \approx 30\ \mu m$ and $N_D \approx 10^{14}\ cm^{-3}$, a compromise between absorption (better than at $20\ \mu m$ in a specular model) and low recombination [8].

Overall, our AM1.5G simulations (specular optics, fixed a-Si:H/c-Si interface, $T = 300\ K$) show that J_{sc} results from an absorption–collection trade-off: it exhibits a quasi-plateau at $\sim 38.4\ mA\ cm^{-2}$ for $e \geq 80\ \mu m$ at low-to-moderate doping (10^{14} – $5 \times 10^{15}\ cm^{-3}$), then decreases when $N_D \gtrsim 5 \times 10^{15}\ cm^{-3}$. The open-circuit voltage V_{oc} remains nearly constant up to $\sim 10^{16}\ cm^{-3}$, then falls for all thicknesses due to recombination (Auger and, in extended models, band-gap narrowing, BGN). The fill factor (FF) peaks at $\sim 86.7\%$ for $e = 20\ \mu m$ under low doping, whereas the efficiency η is maximal at $\sim 25.17\%$ for $e \approx 30\ \mu m$ and $ND \approx 10^{14}\ cm^{-3}$, a compromise between improved absorption (relative to $20\ \mu m$ in a non-textured/specular model) and low recombination losses. Finally, at high doping ($\geq 10^{16}$–$2.5 \times 10^{16}\ cm^{-3}$), rising Auger/BGN simultaneously degrades J_{sc}, V_{oc}, FF, and hence η. These findings will serve as a baseline when, in Section 4.2, we invert the roles to analyze the effect of base thickness e at fixed doping.

We now examine the influence of base thickness e at fixed N_D, in order to disentangle the "absorption/transport" contributions associated with e from those driven by doping.

5. Effect of Base Thickness for Different Base Doping Levels

5.1. Impact on the Short-circuit Current Density (J_{sc})

Figure 8 illustrates the evolution of J_{sc} as a function of the base thickness e $(20 - 400\ \mu m)$ for different donor densities N_D, under AM1.5G, using a specular (non-textured) optical model and a fixed a-Si:H/c-Si interface. This framework highlights the expected absorption–collection trade-off in thinned c-Si and the influence of front-stack losses (TCO/a-Si:H) in modern SHJ devices [4, 5, 13].

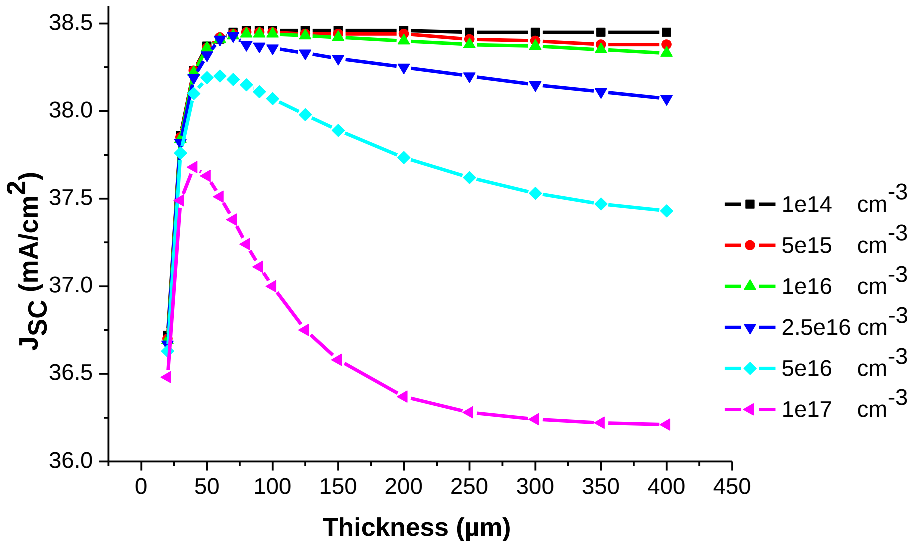

Figure 8. *Variation of the short-circuit current density J_{sc} of an SHJ cell versus thickness e for different values of N_D.*

An examination of Figure 8 reveals that:

1) As thickness increases from 20 to $\sim 70\ \mu m$, J_{sc} rises markedly for all N_D values.
2) Beyond $\sim 70 - 80\ \mu m$, J_{sc} decreases as e increases: the recombination volume (SRH/Auger) grows and outweighs the absorption gain, consistent with non-textured absorption limits [4, 5].
3) The higher the doping N_D, the stronger the drop in J_{sc} at large thickness (shorter lifetimes, reduced diffusion lengths due to Auger) [7].
4) An optimal/plateau value of $J_{sc} \approx 38.46\ mA\ cm^{-2}$ is observed for $N_D = 1 \times 10^{14}\ cm^{-3}$ at thicknesses $\sim 80 - 200\ \mu m$, where absorption is nearly saturated in a non-textured model [4, 13].

Physical interpretation:

1) Thickness effect. Increasing e raises optical generation (more absorbed photons) and hence J_{sc} up to saturation. In a specular (non-Lambertian) model, NIR light remains partly unabsorbed at small e; conversely, at very large e, bulk-collection losses due to recombination become dominant, explaining the subsequent decrease of J_{sc} [4, 5].
2) Doping effect. Increasing N_D reduces resistivity (better conduction) but enhances Auger recombination (and effective SRH), shortening the minority-carrier diffusion length; at very high doping, band-gap narrowing (BGN) is also expected to penalize collection [7, 8].
3) Role of front-stack losses. Parasitic absorption in the front stack (a-Si:H/TCO) limits J_{sc} and helps explain why, even at moderate e, the absorption gain remains bounded without texturing [13].

5.2. Impact on the Open-circuit Voltage (V_{OC})

In our baseline physics deck, the observed V_{oc} roll-off at high N_D is primarily driven by Auger recombination; band-gap narrowing is acknowledged and will be included/calibrated in the extended model, expected to accentuate the high-doping penalty without changing the qualitative trend.

Figure 9 illustrates the evolution of the open-circuit voltage V_{oc} as a function of the base thickness e $(20 - 400\ \mu m)$ for different donor densities N_D, under AM1.5G, using a specular (non-textured) optical model and a fixed a-Si:H/c-Si interface. This framing highlights the link between V_{oc} and the saturation current J_0 (bulk SRH/Auger + interface) via $V_{oc} \simeq (kT/q) ln(J_{sc}/J_0 + 1)$ [6, 19].

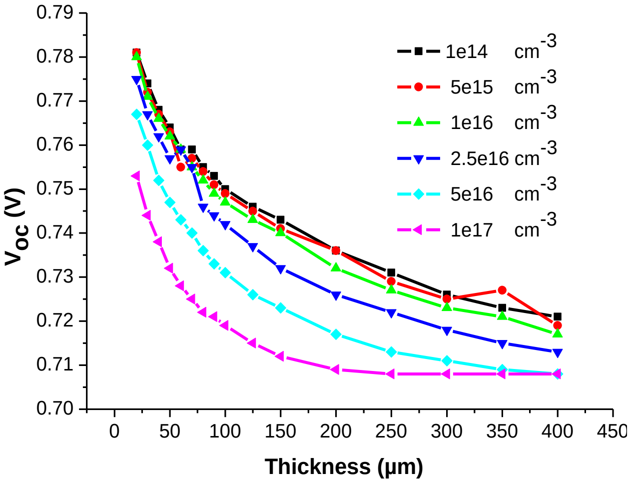

Figure 9. *Variation of the open-circuit voltage V_{oc} of an SHJ cell versus thickness e for different values of N_D.*

Figure 9 shows:

1) For all doping levels, V_{oc} decreases as thickness e increases; for example, at $N_D = 10^{14}\ cm^{-3}$, V_{oc} drops from $0.781\ V$ (at $20\ \mu m$) to lower values as e grows.
2) At a given thickness, the lower the substrate doping, the higher V_{oc}: for $e = 20\ \mu m$, the maximum V_{oc} of $0.781\ V$ is observed for $N_D = 1 \times 10^{14}\ cm^{-3}$ and remains high for $N_D = 5 \times 10^{15}\ cm^{-3}$.
3) The optimal value identified here is $V_{oc} = 0.781\ V$ for $e = 20\ \mu m$ and $N_D = 1 \times 10^{14}\ cm^{-3}$ (also high at $5 \times 10^{15}\ cm^{-3}$).

Physical interpretation.

1) Thickness effect. As e increases, the recombination volume (SRH + Auger) grows, which raises J_0 and reduces V_{oc}. At small thickness, shorter transport paths lower J_0 and support higher V_{oc}, provided front/rear passivation and the interface are of high quality [6].
2) Doping effect. Increasing N_D enhances Auger recombination (strong carrier-concentration dependence) and, in more complete models, band-gap narrowing (BGN); both increase J_0 and thus decrease V_{oc}, irrespective of e [6, 7, 19].
3) Cross-consistency. These trends are consistent with those obtained for J_{sc} (Section 4.2.1): at high N_D, reduced diffusion length and increased Auger recombination simultaneously degrade J_{sc} and V_{oc}, contributing to the observed limits on FF and η (Sections 4.1.3 and 4.1.4) [6-8, 19].

5.3. Impact on the Fill Factor (FF)

Figure 10 shows the evolution of the fill factor (FF) as a function of the base thickness e ($20 - 400\ \mu m$) for different donor densities N_D, under AM1.5G, within a specular (non-textured) optical framework and with a fixed a-Si:H/c-Si interface, a context in which FF results from a trade-off between series resistance, recombination, and the $J - V$ knee near the maximum power point [3, 6, 8, 13, 19].

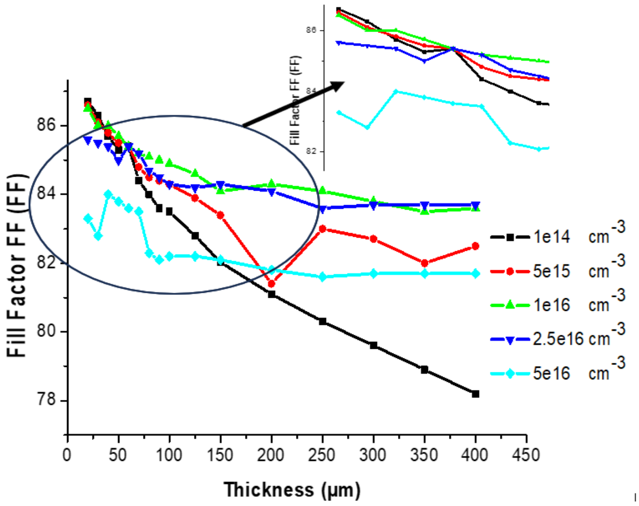

Figure 10. *Variation of the fill factor (FF) of an SHJ cell versus thickness e for different values of N_D.*

An analysis of Figure 10 shows that:

1) For all doping levels, the maximum $FF \simeq 86.7\%$ occurs at $e = 20\ \mu m$; as thickness increases, FF decreases progressively.
2) For large thicknesses, FF is lower when the substrate is very highly doped ($N_D \approx 5 \times 10^{16}\ cm^{-3}$) or very weakly/moderately doped ($N_D \approx 1 \times 10^{14} - 5 \times 10^{15}\ cm^{-3}$); an intermediate doping level generally offers a better compromise.

Physical interpretation

1) Thickness effect. Reducing e lowers the bulk contribution to the series resistance R_s (higher effective base conductivity over a shorter distance) and limits collection losses, which sharpens the $J - V$ knee near the MPP and raises FF; at larger thickness, increased ohmic and bulk-recombination losses degrade the differential slope and thus FF [3, 13, 19].
2) Doping effect. Excessively high doping enhances Auger recombination (and, in more complete models, band-gap narrowing, BGN), which worsens the slope around the MPP and reduces FF [6, 8]. Conversely, too low a doping increases R_s (higher base resistivity) and can limit selective-contact transport, which also penalizes FF [3, 13, 19].
3) Role of the front stack and selective contacts. Parasitic losses and transport barriers in the front stack (a-Si:H/TCO) and at selective contacts influence the $J - V$ shape and thus FF; electrical optimization of these layers is known to significantly increase FF in SHJ devices [3, 13, 19].

5.4. Impact on Efficiency (η)

Figure 11 shows the evolution of the efficiency η as a function of base thickness e $(20-400\ \mu m)$ for different donor densities N_D, under AM1.5G, using a specular (non-textured) optical model and a fixed a-Si:H/c-Si interface. This framework highlights the coupling $\eta = J_{sc}V_{oc}FF/G$ and the characteristic absorption ↔ recombination/transport trade-off in thinned c-Si cells [2, 13].

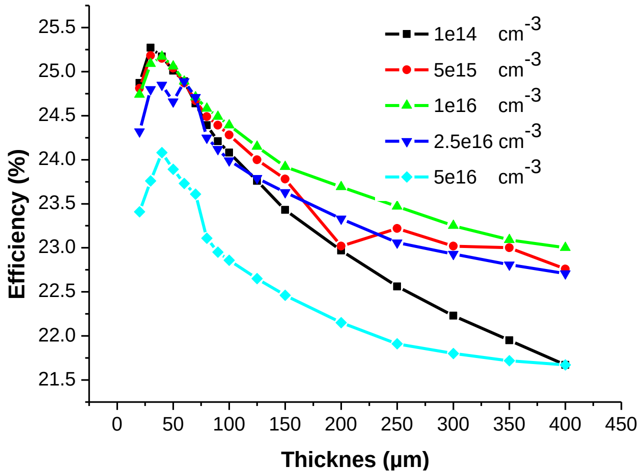

Figure 11. *Variation of the efficiency η of an SHJ cell versus thickness e for different values of N_D.*

An examination of Figure 11 reveals that:

1) For $20-40\ \mu m$ thicknesses, the higher the substrate doping, the lower the efficiency at fixed e, due to increased recombination (Auger/BGN) that degrades V_{oc} and the $J-V$ knee (FF) [7, 8].
2) The optimal efficiency 25.27% is obtained at $e = 30\ \mu m$ for low doping, $N_D = 1\times10^{14} - 5\times10^{14}\ cm-3$.
3) For higher dopings ($N_D = 1\times10^{16}, 2.5\times10^{16}, 5\times10^{16}\ cm^{-3}$), the maximum efficiency shifts to $e \approx 40\ \mu m$; beyond $40\ \mu m$, η decreases for all cells.
4) At large thickness, efficiency is lower when the substrate is very highly doped ($\sim 5\times10^{16}\ cm^{-3}$) or very weakly/moderately doped ($\sim 1\times10^{14} - 5\times10^{15}\ cm^{-3}$; an intermediate doping generally provides the best conduction/recombination compromise.

Physical interpretation

1) Thickness effect. In a specular model, increasing e improves absorption and thus J_{sc} up to saturation (notably in the visible/blue). At very large e, bulk collection losses (SRH/Auger) increase and eventually reduce η; at $e = 20\ \mu m$, NIR remains partly unabsorbed without texturing, explaining why the optimum lies around $30-40\ \mu m$ [4, 13].
2) Doping effect. Raising N_D reduces R_s (higher base conductivity) but strongly increases Auger recombination and, in more complete models, band-gap narrowing (BGN), which lowers V_{oc} and penalizes FF; conversely, too low a doping increase R_s and can limit selective-contact transport. Hence an η optimum at intermediate doping and moderate e [7, 8, 13].
3) Link with J_{sc} and FF. The $\eta \approx 25.27\%$ optimum at $e = 30\ \mu m$ (low N_D) aligns with a high J_{sc} still only mildly penalized by unabsorbed NIR and with FF supported by limited ohmic losses; at high N_D, the optimum that shifts to $e \sim 40\ \mu m$ reflects the balance between improved conduction and increased recombination [4, 7, 8, 13].

Within the fixed framework (specular optics without texturing, constant a-Si:H/c-Si interface, $T = 300\ K$), the cross-analysis of J_{sc}, V_{oc}, FF and η as a function of thickness e and for different dopings N_D highlights:

1) J_{sc} increases as e grows from 20 to $\sim 70-80\ \mu m$, then saturates/declines at larger thickness: without texturing, the absorption gain is eventually offset by bulk collection losses. A quasi-plateau of $\sim 38.4 - 38.5\ mA\ cm^{-2}$ is observed for $N_D = 10^{14}\ cm^{-3}$ in the $80-200\ \mu m$ range.
2) V_{oc} decreases overall with increasing e for all N_D: the larger recombination volume raises J_0 and lowers V_{oc}. At small thickness (e.g., $20\ \mu m$), V_{oc} reaches $\sim 0.781\ V$ at low doping.
3) FF is maximal at $e = 20\ \mu m$ ($\sim 86.7\%$) and then decreases with e; at larger thickness it is degraded by both higher series resistance and increased bulk recombination.
4) Efficiency η shows an optimum at moderate thickness: $\sim 25.27\%$ at $= 30\ \mu m$ $N_D = 10^{14} - 5\times10^{14}\ cm^{-3}$; for higher dopings, the optimum shifts toward $e \approx 40\ \mu m$ and then declines beyond that.
5) The doping effect is ambivalent: increasing N_D lowers R_s (better conduction) but raises Auger recombination (and, in extended models, BGN), which degrades V_{oc}, FF, and hence η. Conversely, too low a doping inflates R_s. Thus, an intermediate N_D combined with moderate e maximizes η.

Limitations & Outlook.

The most impactful limitation is the absence of light-trapping/texturing, which underestimates absolute J_{sc} and η at small e. Two additional simplifications: fixed a-Si:H/c-Si interface and idealized contacts, may shift absolute metrics but not the relative $e - N_D$ trends. We will:

1) add Lambertian/textured optics and ARC,
2) sweep interface defect densities/cross-sections, and
3) include calibrated BGN and contact resistances;

we expect absolute gains with the same design window.

6. Conclusion

Using TCAD (SILVACO ATLAS, $300\ K$, AM1.5G), we investigated the coupled influence of base thickness e and base doping N_D on SHJ cell performance under specular optics (no texturing) with a fixed a-Si:H/c-Si interface. The main findings are:

1) J_{sc} increases from $e = 20$ to $\sim 70 - 80\ \mu m$, then saturates/declines at larger e due to bulk-collection losses; a quasi-plateau of $\sim 38.4 - 38.5\ mA\ cm^{-3}$ appears at low doping for $e \approx 80 - 200\ \mu m$. At $e \approx 30\ \mu m$, J_{sc} remains high in our model because visible-range absorption already dominates and collection benefits from shorter paths, hence efficiency can peak at this thickness despite the absence of texturing.
2) V_{oc} is nearly constant up to $N_D \sim 10^{16}\ cm^{-3}$ and then drops for all thicknesses as doping increases (Auger/BGN); at small e (e.g., $20\ \mu m$) and low doping, we obtain $V_{oc} \approx 0.781\ V$.
3) FF is maximal at $e = 20\ \mu m$ ($\sim 86.7\%$) and decreases with e, due to combined increases in bulk series resistance and recombination.
4) Efficiency shows an optimum at moderate thickness: $\eta \approx 25.2 - 25.3\%$ at $e = 30\ \mu m$ for $N_D = 10^{14} - 5 \times 10^{14}\ cm^{-3}$; for higher dopings, the optimum shifts toward $e \approx 40\ \mu m$ before η declines.

Design implications. A robust operating window emerges around $e = 30 - 40\ \mu m$ with low-to-intermediate doping (avoid $N_D \gtrsim 10^{16}\ cm^{-3}$). In this region, the absorption–transport compromise maximizes η while maintaining high V_{oc} and FF.

Limitations and outlook. We intentionally adopted

1) no texturing (which underestimates J_{sc}, especially at small e), and
2) a fixed interface (which may shift absolute values without changing relative trends).

Future work will incorporate light trapping (texturing/ARC), interface sweeps (defect-state density, capture cross-sections), and refinements (calibrated BGN, realistic metallization/grid and contact resistance, temperature dependence) to raise absolute metrics and refine predictions without overturning the relative trends and the optimal window identified here.

Abbreviations

a-Si	H-Hydrogenated Amorphous Silicon
Al	Aluminum
AM1.5G	Air Mass 1.5 Global spectrum (STC reference)
ARC	Anti-reflective Coating
ATLAS	SILVACO ATLAS Device Simulator
BGN	Band-gap Narrowing
BSF	Back-surface Field
c-Si	Crystalline Silicon
Dit	Interface Defect Density
EQE	External Quantum Efficiency
FF	Fill Factor
FSF	Front-surface Field (p^+ a-Si: H Emitter)
G	Irradiance ($W\ m^{-2}$)
IEC	International Electrotechnical Commission
ITO	Indium Tin Oxide
J	Current Density
J-V	Current-voltage
J_m	Current Density at Maximum Power Point
J_{sc}	Short-circuit Current Density
k_B	Boltzmann Constant
μ_n, μ_p	Electron, Hole Mobility
N_D	Donor Concentration (Base Doping)
n, k	Refractive Index and Extinction Coefficient
NIR	Near-infrared
N_C, N_V	Effective density of states in CB/VB
χ	Electron Affinity
E_g	Band-gap Energy
ε_r	Relative Permittivity
η	Power Conversion Efficiency
PV	Photovoltaic
q	Elementary Charge
R_s, R_{sh}	Series resistance, Shunt Resistance
SRH	Shockley–Read–Hall (Recombination)
STC	Standard Test Conditions ($1000\ W\ m^{-2}$, AM1.5G, 25 ℃)
TCAD	Technology Computer-Aided Design
TCO	Transparent Conductive Oxide
τ_n, τ_p	Electron, Hole Lifetime
σ_n, σ_p	Electron, Hole Capture Cross-section
V_m	Voltage at Maximum Power Point
V_{oc}	Open-circuit Voltage
V_T	Thermal Voltage (kBT/q)

Author Contributions

Jacques Joachim Faye: Conceptualization, Data curation, Formal Analysis, Investigation, Methodology, Software, Validation, Writing – original draft, Writing – review & editing

Aly Toure: Conceptualization, Data curation, Formal Analysis, Investigation, Methodology, Software, Validation, Writing – original draft, Writing – review & editing

Mamadou Lamine Samb: Conceptualization Data curation, Formal Analysis, Investigation, Methodology, Project administration, Resources, Software, Supervision, Validation, Visualization, Writing – original draft, Writing – review & editing

Dimity Diassy: Conceptualization, Data curation, Formal Analysis, Investigation, Methodology, Software, Validation, Writing – original draft, Writing – review & editing

Conflicts of Interest

The authors declare no conflicts of interest.

References

[1] Green, M. A., et al. "Solar cell efficiency tables (version 63)." *Prog. Photovolt: Res. Appl.* (2024). https://doi.org/10.1002/pip.3750

[2] Boccard, M., Holman, Z. C. "Passivating contacts for crystalline Si solar cells." *Nat. Energy* 5, 951–964 (2020).

[3] Green, M. A.; Dunlop, E. D.; Hohl-Ebinger, J.; Yoshita, M.; Kopidakis, N.; Hao, X. Solar cell efficiency tables (version 62). *Progress in Photovoltaics: Research and Applications.* 2023, 31(5), 527–542. https://doi.org/10.1002/pip.3726

[4] Lin, H.; et al. Silicon heterojunction solar cells with up to 26.81% efficiency achieved by electrically optimized nanocrystalline-silicon hole contact layers. *Nature Energy.* 2023, 8, 789–799. https://doi.org/10.1038/s41560-023-01255-2

[5] Andreani, L. C.; et al. Silicon solar cells: Toward the efficiency limits. *Advanced Physics: X.* 2019, 4(1), 1548305. https://doi.org/10.1080/23746149.2018.1548305

[6] Saive, R. Light trapping in thin silicon solar cells: A review on fundamentals and technologies. *Progress in Photovoltaics.* 2021, 29(10), 1125–1137. https://doi.org/10.1002/pip.3440

[7] Richter, A.; et al. Improved parameterization of Auger recombination in crystalline silicon. *Journal of Applied Physics.* 2013, 113, 053707. https://doi.org/10.1063/1.4789814

[8] Yan, D.; Cuevas, A. Empirical determination of the energy band-gap narrowing in heavily doped silicon. *Journal of Applied Physics.* 2014, 116, 194505. https://doi.org/10.1063/1.4902066

[9] Rawa, M.; et al. Single-diode PV models and analytical/Lambert-W solutions: A review. *Sensors.* 2022, 22, 4173. https://doi.org/10.3390/s22114173

[10] Green, M. A. Accurate expressions for solar cell fill factors including series and shunt resistances. *Applied Physics Letters.* 2016, 108, 081111. https://doi.org/10.1063/1.4942660

[11] IEC 60904-3: 2019: Photovoltaic devices: Part 3: Measurement principles for terrestrial PV devices with reference spectral irradiance data (AM1.5G, STC). International Electrotechnical Commission, 2019. Available from: https://webstore.iec.ch/ (accessed 7 Oct 2025).

[12] Adaine, A. Numerical optimization of very high-efficiency InGaN-based solar cells. Ph.D. Thesis, University of Lorraine, Nancy, France, 2018.

[13] Holman, Z. C.; et al. Current losses at the front of silicon heterojunction solar cells. *IEEE Journal of Photovoltaics.* 2012, 2(1), 7–15. https://doi.org/10.1109/JPHOTOV.2011.2174967

[14] Yoshikawa, K.; et al. Silicon heterojunction solar cell with interdigitated back contacts for a photoconversion efficiency over 26%. *Nature Energy.* 2017, 2, 17032. https://doi.org/10.1038/nenergy.2017.32

[15] Bestelink, E.; Sihapitak, P.; Zschieschang, U.; et al. High gain complementary inverters based on comparably-sized IGZO and DNTT source-gated transistors. *Journal of Materials Chemistry C.* 2023, 11(34), 11688–11696. https://doi.org/10.1039/D3TC02474A

[16] Alipour, A.; Alipour, H. Device modeling of high performance and eco-friendly FAMASnI3_33-based perovskite solar cell. *Scientific Reports.* 2024, 14, 14425. https://doi.org/10.1038/s41598-024-66485-0

[17] Boukortt, N. E. I.; Patanè, S.; AlAmri, A. M.; et al. Numerical Investigation of Perovskite and u-CIGS Based Tandem Solar Cells Using Silvaco TCAD Simulation. *Silicon.* 2023, 15, 293–303. https://doi.org/10.1007/s12633-022-01960-9

[18] Andreani, L. C.; Bozzola, A.; Kowalczewski, P.; Liscidini, M.; Redorici, L. Photonic light trapping and electrical transport in thin-film crystalline Si solar cells. *Solar Energy Materials and Solar Cells.* 2015, 135, 78–92. https://doi.org/10.1016/j.solmat.2014.10.012

[19] Varache, R.; Leendertz, C.; Gueunier-Farret, M. E.; Haschke, J.; Muñoz, D.; Korte, L. Investigation of selective junctions using a newly developed tunnel current model for solar cell applications. *Solar Energy Materials and Solar Cells.* 2015, 141, 14–23. https://doi.org/10.1016/j.solmat.2015.05.014

[20] Tamang, A.; et al. Enhanced photon management in silicon thin-film solar cells by separate optimization of front and back textures. *Scientific Reports.* 2016, 6, 29639. https://doi.org/10.1038/srep29639

[21] PV-Tech / LONGi. LONGi sets 26.81% efficiency record for heterojunction solar cells. News article, Nov 21, 2022. Available from: https://www.pv-tech.org/longi-sets-26-81-efficiency-record-for-heterojunction-solar-cells/